

This is the author's final, peer-reviewed manuscript as accepted for publication (AAM). The version presented here may differ from the published version, or version of record, available through the publisher's website. This version does not track changes, errata, or withdrawals on the publisher's site.

Impact of 1,8-diiodooctane on the morphology of organic photovoltaic (OPV) devices – A Small Angle Neutron Scattering (SANS) study

Gabriel Bernardo, Hugo Gaspar, Gabriel E. Pérez, Alec S. D. Shackelford, Andrew J. Parnell, Markus Bleuel, Adélio Mendes, Stephen M. King, Steven R. Parnell

Published version information

Citation: G Bernardo et al. "Impact of 1,8-diiodooctane on the morphology of organic photovoltaic (OPV) devices – a Small Angle Neutron Scattering (SANS) study." *Polymer Testing*, vol. 82 (2020): 106305.

DOI: [10.1016/j.polymertesting.2019.106305](https://doi.org/10.1016/j.polymertesting.2019.106305)

©2019. This manuscript version is made available under the [CC-BY-NC-ND](https://creativecommons.org/licenses/by-nc-nd/4.0/) 4.0 Licence.

This version is made available in accordance with publisher policies. Please cite only the published version using the reference above. This is the citation assigned by the publisher at the time of issuing the AAM/APV. Please check the publisher's website for any updates.

This item was retrieved from **ePubs**, the Open Access archive of the Science and Technology Facilities Council, UK. Please contact epubs@stfc.ac.uk or go to <http://epubs.stfc.ac.uk/> for further information and policies.

Impact of 1,8-diiodooctane on the morphology of organic photovoltaic (OPV) devices – A Small Angle Neutron Scattering (SANS) study

Gabriel Bernardo^{1,2,*}, Hugo Gaspar¹, Gabriel E. Pérez³, Alec S. D. Shackelford⁴, Andrew J. Parnell¹, Markus Bleuel⁵, Adélio Mendes², Stephen M. King⁶, Steven R. Parnell⁷

¹Department of Physics and Astronomy, University of Sheffield, S3 7RH, UK

²*LEPABE*, Department of Chemical Engineering, University of Porto, 4200-465 Porto, Portugal

³Department of Chemical and Biological Engineering, University of Sheffield, S1 3JD, UK

⁴Department of Mechanical Engineering, University of Sheffield, S3 7QB, UK

⁵NIST, Centre for Neutron Research, Gaithersburg, MD 20899 USA

⁶ISIS Pulsed Neutron and Muon Source, STFC, Rutherford Appleton Laboratory, Harwell Campus, Didcot, Oxon, OX11 0QX, UK

⁷Faculty of Applied Sciences, Delft University of Technology, Mekelweg 15, 2629 JB Delft, Netherlands

Corresponding author: gbernardo@fe.up.pt

Abstract

The impact of the additive 1,8-diiodooctane on the morphology of bulk-heterojunction solar cells based on the systems P3HT:PC₇₁BM, PTB7:PC₇₁BM and PTB7-Th:PC₇₁BM is studied using a combination of Small Angle Neutron Scattering (SANS) and Atomic Force Microscopy (AFM). The results clearly show that while in the P3HT:PC₇₁BM system, the additive DIO promotes a slight coarsening of the phase domains (type I additive), in the systems PTB7:PC₇₁BM and PTB7-Th:PC₇₁BM, DIO promotes a large decrease in the size of the phase domains (type II additive). SANS is demonstrated as being particularly useful at detecting the minor morphological changes observed in the P3HT:PC₇₁BM system, which can be hardly seen in AFM. This work illustrates how SANS complements AFM and both techniques when used together provide a deeper insight into the nanoscale structure in thin organic photovoltaic (OPV) device films.

1. Introduction

Organic photovoltaics (OPVs) represent a very promising approach to generate renewable energy [1-4]. Compared to silicon-based solar cells, OPVs can be manufactured from solution over much larger areas on flexible and lightweight plastic substrates using high-throughput roll-to-roll (R2R) compatible processing technologies [5] leading to considerable reductions in fabrication cost. In the last decade OPVs have developed steadily, recently attaining power conversion efficiencies (PCE) in the range 14 – 16.5 % for single junction devices [6-8] and PCE >17% for tandem devices [9]. These high PCE values, in combination with reported device lifetimes >10,000 hours [10], place the technology on the verge of economic viability and full commercial rollout.

The active layer of an OPV device consists of an intermixed blend of donor (usually conjugated polymers [11]) and acceptor (either fullerenes [4] or non-fullerene small-molecules [12]) materials, with domain sizes in the nanometre range, the so-called bulk-heterojunction (BHJ). The PCE of OPVs is strongly dependent on the morphology within the BHJ film and solvent additives, such as 1,8-Diiodooctane (DIO), are usually added to the casting solution to optimize the BHJ morphology [13, 14]. Rather than changing the aggregation state of fullerene in solution [15, 16] as once thought, the role of additives like DIO is to plasticize the thin BHJ film and change its drying kinetics [15-17]. The morphological effects of additives depend both on the additive and on the specific type of BHJ system under investigation. These morphological effects can be classified as either increasing phase separation (type I) or suppressing oversized phase separation (type II) [13].

Conjugated polymers such as P3HT, PTB7 and PTB7-Th, and fullerenes such as PC₇₁BM, are formed by light atoms such as C, H, O, S and F. But electron beams (and X-rays) interact with atomic electrons meaning that the greatest contrast is obtained between elements of significantly different atomic numbers and regions where atoms are more densely packed. Therefore, although electron-based techniques such as Transmission Electron Microscopy (TEM) can offer enough phase contrast between crystalline polymer-fullerene regions, they usually fail to distinguish between the amorphous regions. On the other hand, although AFM techniques can probe the morphology of film surfaces, this might be very different from the morphology of the underlying bulk film. For these reasons, classifying the morphological effect of additives (type I or type II), using common techniques such as AFM and TEM, can be

sometimes difficult and misleading and some contradictory observations have been reported in the literature as detailed below.

Arca *et al.* [18] and Jang *et al.* [19], using AFM, reported that the addition of DIO to P3HT:PC₆₁BM and to P3HT:PC₇₁BM bulk-heterojunctions, increases the size of phase domains (type I additive) and the roughness of the films. Additionally, Arca *et al.* [18] correlated this domain coarsening, promoted by DIO, to the observed increase in the PCE of P3HT:PC₆₁BM devices from 3.7% to 4.9%. Long *et al.* [20] using time-resolved fluorescence spectroscopy, studied the effect of DIO on the morphology of P3HT:PC₆₁BM and P3HT:PC₇₁BM BHJs. In the case of P3HT:PC₆₁BM BHJs, the authors observed a decrease in the rate of fluorescence quenching, in films processed with DIO, suggesting an increase in phase separation (type I additive) in agreement with the observations by Arca *et al.* [18]. In the case of P3HT:PC₇₁BM blends a faster fluorescence quenching was observed in DIO processed films, suggesting better mixing and smaller phase domains (type II additive), contrary to the observations by Jang *et al.* [19].

Liang *et al.* [21] used transmission electron microscopy (TEM) to study the impact of DIO on the morphology of PTB7:PC₇₁BM BHJ. Large domains (about 100–200 nm in diameter) were observed in the BHJ processed without DIO. By contrast, the BHJ prepared from CB/DIO exhibited a much more uniform morphology with good mixing between PTB7 and PC₇₁BM (type II additive). Huang *et al.* [22], using AFM, identified large PC₇₁BM rich domains with dimensions from ~50 to 300 nm and a root mean-square (*rms*) roughness of 6.58 nm, in PTB7:PC₇₁BM BHJ prepared without additive. The film processed using DIO as additive was much smoother (*rms* roughness = 1.27 nm) suggesting a better mixing (type II).

Wan *et al.* [23] studied the effect of DIO on the size of phase domains of the BHJ of PTB7-Th:PC₇₁BM devices using Resonant Soft X-ray Scattering (RSoXS). RSoXS scattering peaks, with and without DIO, at similar scattering vector q locations indicated that DIO does not significantly alter the phase separation length scale. However, the values of the total scattering intensity (TSI), which are directly proportional to the domain purity, indicated that the domain purity with 3% DIO was higher (TSI = 0.95) than without DIO (TSI = 0.91). AFM *rms* roughness values were 1.20 and 0.70 with and without DIO respectively. More recently, Xie *et al.* [24] and Huang *et al.* [25] have reported results that strongly support the role of DIO as a type II additive in PTB7-Th:PC₇₁BM BHJs and that differ considerably from the results of Wan *et al.* [23]. Using AFM and TEM, Xie *et al.* [24] have shown that a PTB7-Th:PC₇₁BM

film processed without DIO contains large domains of about 200 nm in diameter and a *rms* roughness = 4.37 nm. By contrast films prepared with DIO have no large phase separation and tend to form interpenetrating networks with smoother surfaces (*rms* roughness = 2.17 nm). In agreement with this, Huang *et al.* [25] also observed that films of PTB7-Th:PC₇₁BM processed without DIO contained considerably larger domain sizes (146 nm) than the corresponding films processed with DIO (32.5 nm).

One clear advantage of the use of Small-Angle Neutron Scattering (SANS), compared to AFM and TEM, is that SANS is a bulk sampling technique and, due to the intrinsically very different neutron scattering length densities (SLD) between hydrogen-containing polymers and hydrogen-deficient fullerenes, there is a high contrast between these phase regions, irrespective of their crystallinity. Thus, whilst SANS measurements do not provide the same visually-intuitive picture of a sample that TEM and AFM do, they are sensitive to structural information that TEM and AFM simply are not. However, despite these advantages, the use of SANS in OPV research has been patchy.

One limitation of SANS is that a single BHJ thin film, with a typical thickness in the range 100 – 300 nm, is too thin to generate a scattering signal with good signal-to-noise in a practical timespan. Although the use of a thick solvent-cast polymer-fullerene film, as previously considered by some authors [26, 27], can solve this instrumental limitation, it is unsatisfactory because the morphology of a thick solvent cast film is not necessarily representative of the morphology of a thin BHJ film as used in a functioning OPV device because of interfacially-driven processes. An alternative approach, that we have previously reported [17, 28], consists of using stacks of thin BHJ films deposited on synthetic (and so non-crystalline) quartz discs. Quartz is essentially transparent to neutrons and contributes very little background signal. This approach can guarantee enough material in the beam to generate good signal-to-noise, while simultaneously preserving the thin film and representative “device like” morphology.

In the present work we extend our previous study on the impact of DIO on the morphology of BHJs [17] to other common polymer-fullerene systems (P3HT:PC₇₁BM [18-20]; PTB7:PC₇₁BM [21, 22, 29] and PTB7-Th:PC₇₁BM [23-25, 29]), and we use SANS and AFM as the investigative techniques. Our main goal was to assess SANS, and its complementarity to AFM, as a probe of the morphology of polymer:fullerene bulk-heterojunction solar cells.

2. Experimental Part

2.1 Materials

The chemical structures of the polymers and fullerene (all purchased from Ossila Ltd), used in this work, are shown in Figure 1 and they are: a) Poly(3-hexylthiophene-2,5-diyl) commonly known as P3HT (batch M102, RR= 95.7%, $M_w = 65,200 \text{ g.mol}^{-1}$, $M_n = 29,600 \text{ g.mol}^{-1}$, PDI = 2.2); b) Poly[[4,8-bis[(2-ethylhexyl)oxy]benzo[1,2-b:4,5-b']dithiophene-2,6-diyl][3-fluoro-2-[(2-ethylhexyl)carbonyl]thieno[3,4-b]thiophenediyl]], commonly known as PTB7 ($M_w = 18,000 \text{ g.mol}^{-1}$, $M_n = 10,500 \text{ g.mol}^{-1}$, PDI = 1.75); c) Poly[4,8-bis(5-(2-ethylhexyl)thiophen-2-yl)benzo[1,2-b:4,5-b']dithiophene-2,6-diyl-alt-(4-(2-ethylhexyl)-3-fluorothieno[3,4-b]thiophene-)-2-carboxylate-2,6-diyl]], commonly known as PTB7-Th or PBDTTT-EFT ($M_w > 40,000 \text{ g.mol}^{-1}$, $M_n > 20,000 \text{ g.mol}^{-1}$, PDI = 1.8 – 2.0); d) [6,6]-Phenyl-C71-butyric acid methyl ester (PC₇₁BM) (batch M113, 95% PC₇₁BM with 5% PC₆₁BM).

The solvents chlorobenzene (anhydrous 99.8%) and 1,8-diiodooctane (98%) were purchased from Sigma-Aldrich and used as received.

2.2 Sample Preparation

Solutions were prepared in chlorobenzene containing the following polymer:fullerene mass ratios, as used in the corresponding optimised OPV devices: P3HT:PC₇₁BM (3:2); PTB7:PC₇₁BM (1:1.5) and PTB7-Th:PC₇₁BM (1:1.5). The solutions were prepared inside a glovebox and left stirring overnight in a hotplate at 90 °C.

For SANS characterization, films were spun-cast on 0.5 mm thick Spectrosil™ quartz discs (Knight Optical WHQ 1500-C) (15 mm diameter) that had been pre-coated with a layer of PEDOT:PSS (~40 nm). The SANS from a selection of the discs was measured before spin-casting in order to confirm the discs themselves would not contribute artefacts to the scattering.

For each polymer:PC₇₁BM system, three types of thin BHJ films were prepared, replicating exactly the same preparation procedure that we have previously used in the preparation of OPV devices [17]: i) films spun-cast from a solution without DIO which were subsequently left drying inside the glovebox for ~2 hours before being fully dried under Ultra-High-Vacuum (UHV) at $\sim 5 \times 10^{-6}$ mbar ; ii) films spun-cast from a solution with 3 v/v% DIO which were subsequently left drying inside the glovebox for ~2 hours before being fully dried under UHV at $\sim 5 \times 10^{-6}$ mbar; iii) films spun-cast from a solution with 3 v/v% DIO which were left drying inside the glovebox for ~2 hours, subsequently annealed on a hotplate for 5 minutes

at 100 °C under N₂ atmosphere inside the glovebox and finally fully dried under UHV at $\sim 5 \times 10^{-6}$ mbar. We note that under UHV conditions the additive DIO is completely removed from the corresponding films [17]. For each film:preparation combination, 14 quartz discs with a single film were prepared. All the completely dried films (each with an average thickness of ~ 100 nm) were then removed from the UHV chamber, each type of film was then assembled into stacks of 14 discs, placed inside appropriate sample holders and stored for later characterization. The creation of stacks with 14 films per stack had previously been found to generate good signal-to-noise in the SANS measurements, while still using the same conditions as used in the preparation of devices.

2.3 Sample Characterisation

SANS data from the stacks of solid thin films were acquired on the LOQ and SANS2D “white beam” time-of-flight diffractometers at the ISIS Pulsed Neutron Source (Didcot, UK). In a SANS experiment, the normalized intensity (I) of scattered neutrons per unit sample volume V is measured as a function of scattering vector (or momentum transfer) $q = (4\pi/\lambda)\sin\theta/2$, where λ is the neutron wavelength and θ is the scattering angle. The intensity arising from N homogeneous isotropic scatterers of volume V_s and scattering length density ρ_s , dispersed in a polymer of scattering length density ρ_p is

$$I(q) = \phi_s V_s (\rho_s - \rho_p)^2 P(q) S(q) \quad (1)$$

where $\phi_s = NV_s$ is the volume fraction of scatterers, the function $P(q)$ is the form factor describing the size and shape of the scatterers, and $S(q)$ is the structure factor describing interactions between the scatterers. The term in brackets, the square of the difference in SLD values between the scatterers and the matrix, is known as the contrast.

Due to the high carbon to hydrogen content in PC₇₁BM, there is a naturally high neutron scattering length density contrast with the hydrogenous polymers P3HT, PTB7 and PTB7-Th that removes the usual need for isotopic substitution (e.g. deuteration). More specifically, the scattering length density of PC₇₁BM is $\text{SLD}(\text{PC}_{71}\text{BM}) = 4.42 \times 10^{-6} \text{ \AA}^{-2}$ and the corresponding values for the three polymers considered in this work are $\text{SLD}(\text{P3HT}) = 0.614 \times 10^{-6} \text{ \AA}^{-2}$, $\text{SLD}(\text{PTB7}) = 0.911 \times 10^{-6} \text{ \AA}^{-2}$ and $\text{SLD}(\text{PTB7-Th}) = 0.995 \times 10^{-6} \text{ \AA}^{-2}$.

LOQ [30] is a fixed-geometry instrument which utilizes a neutron beam modulated at 25 Hz and having a wavelength range between 2 Å and 10 Å. Data are simultaneously recorded on two, two-dimensional, position-sensitive neutron detectors, to provide a simultaneous

measure of scattering over the q -range $0.008\text{--}1.6 \text{ \AA}^{-1}$. SANS2D [31] is a higher flux, variable-geometry, instrument that provides a simultaneous q -range of $\sim 0.0016\text{--}0.5 \text{ \AA}^{-1}$ using neutron wavelengths between 1.7 \AA and 16.5 \AA at 10 Hz.

Each sample stack and associated background sample were typically measured for 1 to 2 hours in order to collect data of suitable statistical quality. A reference sample stack, with a PEDOT:PSS layer deposited in each of the 14 quartz discs, was also measured as a background. Each raw scattering data set was then radially-averaged, corrected for the detector efficiency, sample transmission and background scattering and then converted to scattering cross-section data on an absolute scale ($\partial\Sigma/\partial\Omega$ vs q) using the Mantid framework [32]. Intensity calibration was performed by measuring a secondary standard (a blend of hydrogenous and perdeuterated polystyrene of known molecular weight) in accordance with established protocols [33]. For convenience, we shall follow the normal convention of referring to $\partial\Sigma/\partial\Omega$ as intensity (I). The corrected data were then fitted to appropriate models using the SasView software (Version 4.1.1) [34].

For comparison with the SANS data, Scanning Force Microscopy (Dimension 3100, Veeco) in tapping mode was also used to image the surface morphology of the bulk-heterojunction thin films with and without DIO and after thermal annealing. These films were taken from the same batch as the films studied with SANS.

3. Results and Discussion

Figure 2 shows the SANS profiles recorded from a stack of P3HT:PC₇₁BM blend films on quartz discs on the LOQ instrument, with intensity plotted versus scattering vector. It is worth noting that, in absolute terms, the SANS intensities from all the film stacks are very small, and the error bounds depicted are dominated by the (Poisson) counting statistics during the data collection. As shown in Figure 2, the two samples processed with DIO have ~5 times more scattering intensity in the low- q region than the sample processed without DIO. Furthermore, the sample processed with DIO and annealed for 5 minutes at 100 °C has a higher scattering intensity than the unannealed sample processed with DIO. Together, these observations indicate that adding DIO, or adding DIO and then annealing the films, brings about a change in the number of scatterers and/or their effective volume. In other words, Figure 2 is evidence of changes in the underlying nanostructure of the films. To try and quantify these changes, the data in the q range from 0.008 – 0.1 Å⁻¹ was fitted using the Debye-Anderson-Brumberger (DAB) (also known as the Debye-Bueche (DB)) model. This model has been used previously by us [17, 28] for the system PffBT4T-2OD:PC₇₁BM and by Chen *et al.* [35] for the P3HT:PC₆₁BM system, and describes the scattering from a randomly-distributed, two-phase system that is characterized by a single length scale – a density correlation length, L . This is a measure of the average spacing between two regions of the same phase. The model assumes a smooth interface between the two phases. The DAB function has the form

$$I(q) = C_{DAB} \frac{L^3}{(1 + (qL)^2)^2} + b \quad (2)$$

where the scaling factor $C_{DAB} = 8\pi(\Delta\rho)^2 \phi_s(1-\phi_s)$ and $\Delta\rho$ is the neutron contrast. The second term on the right hand side of the equation (b) is the background intensity that includes both instrumental and sample specific factors, e.g. the incoherent scattering intensity. The values obtained from the fitting for C_{DAB} and L using Equation 2 are given in Table 1. Also shown are the corresponding values of the normalized χ^2 . As shown in Figure 2(a), the DAB model gives a reasonably good description of all the data (solid lines) and this is confirmed by the low values of the normalized χ^2 in Table 1. According to the DAB model fitting, a spun-cast sample without DIO and without annealing has a correlation length of ~4.1 nm. Upon addition of 3% DIO to the casting solution the correlation length increases to ~5.7 nm and a further increase in correlation length to ~6.4 nm is observed when the sample containing DIO is annealed for 5

minutes at 100 °C. We note that these correlation lengths are similar to those previously reported for a P3HT:PC₆₁BM system upon annealing at 150 °C [35]. Interestingly, we also note that the effects of DIO and annealing that we observe in this P3HT:PC₇₁BM system are identical to those that we have reported previously [17] for the system PffBT4T-2OD:PC₇₁BM in the sense that both DIO and annealing contribute to an increase in the size of the phase domains, and the system with higher phase coarsening is the one in which both DIO and annealing have been used.

$$I(q) = \phi_s(1 - \phi_s)V_s(\Delta\rho)^2 \left[\frac{3 \sin(qR) - qR \cos(qR)}{(qR)^3} \right]^2 + b \quad (3)$$

The SANS profiles from stacks of PTB7:PC₇₁BM blend films measured on the LOQ instrument are shown in Figure 3(a) and the corresponding AFM images in Figure 3(b). The scattering profile from the sample without DIO is very different from the other two samples (and from the P3HT no-DIO sample). Though it can be represented by the DAB model there are significant uncertainties on all parameters which does not lend confidence to the optimised solution. The gradient of these data for $q < 0.024 \text{ \AA}^{-1}$ is q^{-m} with $m \sim 3.8$ which indicates well-defined interfacial segregation that clearly extend to length scales outside the q -range of LOQ. These length scales d must be therefore larger than $d = 2\pi/q_{\min} \approx 78.5 \text{ nm}$. These data can, however, be modelled as essentially monodisperse, homogeneous spheres (Equation 3) of diameter $2R \sim 182 \text{ nm}$, although the volume fraction of scatterers ϕ_s seems unrealistically low. This finding is supported by the AFM image in Figure 3(b) which shows that the film processed without DIO exhibits coarse phase segregation with large spherical structures, $\sim 200 \text{ nm}$ in size, in agreement with previous reports [21], with a *rms* roughness of 2.6 nm. By contrast, in the films processed with DIO the morphology is visually much smoother with much smaller phase domains, also in agreement with previous reports [21]. This is especially true in the unannealed film processed with DIO which has an *rms* roughness of 0.89 nm. Upon annealing the morphology coarsens slightly to an *rms* roughness of 1.32 nm. The SANS from these PTB7:PC₇₁BM blend films can be adequately represented by the DAB model as before. The fit parameters are given in Table 2.

In order to get a more complete understanding of the scattering of the PTB7:PC₇₁BM sample without DIO we have re-measured the same stack to lower q on the SANS2D instrument. The data are shown in Figure 4. Once again the form of the data was much better described by a homogeneous spheres model than by the DAB model although, as shown by the

black line on Figure 4 and in the lower part of Table 2, it was necessary to assign a greater degree of size polydispersity (PD) to the scatterers: fitted PD ratio = 0.33 using a lognormal distribution. The fitted diameter of the spheres was essentially identical to the value obtained from the narrower q -range data. However, as can be seen, the sphere model does not reproduce an apparent ‘turn-over’ in the data at very low q -values. Unfortunately, the data are insufficient to say if this ‘turn-over’ is a genuine plateauing of the intensity or one side of a peak corresponding to a phase dimension of $d \sim 400$ nm. We shall return to this point shortly.

Figure 5(a) shows the SANS profiles for the stacks of PTB7-Th:PC₇₁BM blend films. The corresponding AFM images are shown in Figure 5(b). The SANS profiles observed for these PTB7-Th:PC₇₁BM films are similar to those observed in the PTB7:PC₇₁BM system. In the PTB7-Th:PC₇₁BM system the scattering from the sample without DIO is also very different from the samples with DIO. But, in this case, the sample without DIO shows a gradient q^m with $m \sim 3.0$ in the q -range for $q < 0.034 \text{ \AA}^{-1}$. This indicates a considerably greater degree of interfacial roughness than in the PTB7 case. In contrast to our experience with the PTB7 system, we have been able to fit all the PTB7-Th data to the DAB model. The results are shown as solid lines on Figure 5(a) and the model parameters are given in Table 3. The BHJ sample processed without DIO exhibits a relatively large correlation length of 18.4 nm but this decreases considerably to 3.7 nm and 5.2 nm in the samples processed with DIO (non-annealed and annealed respectively). These results are in good agreement with the AFM images in Figure 5(b), which clearly show that the film processed without DIO is quite coarse: the *rms* roughness is 1.6 nm. In the non-annealed film processed with DIO the morphology is smoother with smaller phase domains and an *rms* roughness of 0.96 nm. Upon annealing of the film processed with DIO the morphology again coarsens to an *rms* roughness of 1.6 nm. A simple visual observation of the AFM images of both films processed with DIO (non-annealed and annealed) suggests however that both have very similar phase domain sizes.

We have also re-measured the PTB7-Th stack processed without DIO on the SANS2D instrument and those data are also shown in Figure 4. This time a more clearly resolved peak is apparent at $q \approx 0.004 \text{ \AA}^{-1}$, corresponding to a phase dimension $d \sim 157$ nm. We have fitted this extended profile using the DAB model and the results are shown in Table 3 and plotted as solid red line in Figure 4. As shown in Table 3, in this scenario the fitted correlation length obtained was 23.5 nm, which is also in good qualitative agreement with the corresponding AFM image. However, once again, the DAB model is unable to fit the peak. But, in this instance the homogeneous spheres model was also unsatisfactory (because the limiting

behaviour of Equation 3 at small qR is q^{-4} and not q^{-3}). Alternative explanations for the origin of the peaks in the unannealed PTB7:PC₇₁BM and PTB7-Th:PC₇₁BM films without DIO are therefore necessary.

According to recent work, there is a growing evidence in the literature that many polymer:fullerene and other polymer:small-molecule systems may phase separate by a spinodal mechanism [36, 37]. Spinodal decomposition (SD), as it is known, is a diffusion-controlled process well-known for generating nanostructure in multi-phase liquids, metal alloys, glasses, and mixed polymer systems, and differs from conventional nucleation and growth (NG) processes in that it is characterised by compositional fluctuations (with a ‘wavelength’ Ψ) that form spontaneously due the absence of a free energy barrier. A number of functions have been proposed to describe the scattering from SD in particular types of system, both far from, and close to, what is termed the percolation threshold. Whilst many of these functions have the ability to provide quite detailed insights, it is not obvious which of them might be a realistic description of SD in a polymer:fullerene system. However, there is a generic phenomenological description due to Furukawa [38] given by Equation 4.

$$I(q) = C_{SD} \frac{(1 + \gamma/2)x^2}{(\gamma/2) + x^{(2+\gamma)}} + b \quad (4)$$

where $x = q/q_0$, q_0 is the peak position, $\Psi = 2\pi/q_0$, and the exponent γ is related to both the dimensionality of the system and how close the system is to the percolation threshold. We have tried model-fitting this function to the SANS data from our unannealed PTB7:PC₇₁BM and PTB7-Th:PC₇₁BM films without DIO and the results are shown in Tables 3 and 4, and Figure 4. Although the SD model is able to reproduce the peak in the PTB7-Th:PC₇₁BM data it is no better at describing the remainder of the data than the DAB model. And in the case of PTB7:PC₇₁BM the SD model is, if anything, slightly worse at describing these data than the homogeneous spheres model. However, the values of γ returned from the fitting, ~ 4.5 for PTB7:PC₇₁BM and ~ 3.4 for PTB7-Th:PC₇₁BM are intriguing. According to Furukawa, if the phase boundary is ‘smooth’ then one would expect $\gamma = 3$ in two-dimensions or $\gamma = 4$ in three-dimensions, whereas if the phase boundary is ‘rough’ then one would expect $\gamma = 4$ in two-dimensions or $\gamma = 6$ in three-dimensions. If we assume that our thin films are ‘two-dimensional’ then the inference from the SD model-fitting is that there is greater interfacial roughness, over longer length scales, in the PTB7:PC₇₁BM system. This is consistent with our AFM data.

Nonetheless, a definitive model description of the nanostructure in these two systems remains elusive.

It is important to make a few comments about the complementarity of SANS and AFM for assessing nanocomposite morphology. Whilst AFM is arguably a more accessible technique than SANS, it nonetheless has some drawbacks. First, there is the issue of the representative nature of the sampling process. While AFM is a surface technique, SANS is a technique that, due to the highly penetrating nature of neutrons, probes the bulk of the sample and, as vastly reported in the OPV literature [39], the bulk morphology of a thin BHJ film may be very different from its surface morphology. Furthermore, the sampling area in SANS is much larger than in AFM, and therefore more representative of the whole sample. For example, in the present work we have used a 10 mm diameter neutron beam, meaning an illuminated area $\sim 78 \text{ mm}^2$ per window. As we have used stacks of 14 windows the total illuminated area per stack was $\sim 11 \text{ cm}^2 (= 1.1 \times 10^9 \text{ } \mu\text{m}^2)$. However, in the AFM pictures shown in Figures 2(b), 3(b) and 5(b) the maximum area probed in a single picture is only $\sim 9 \text{ } \mu\text{m}^2$. Secondly, there is the issue of phase contrast. In SANS, the phase contrast stems from the neutron-nucleus interaction and can be very different between nuclei of similar atomic number, as it indeed is between carbon and hydrogen. Thus, whilst our SANS measurements do not provide the same visually-intuitive picture of a sample that AFM does, they are sensitive to buried structural information that AFM simply is not. This is particularly relevant in distinguishing very small morphological differences, such as just a few nanometres change in the size of phase domains, as for example reported in this work for the system P3HT:PC₇₁BM.

In Figure 6 we present the correlation between the size of polymer:fullerene phase domains and the PCE of the corresponding devices as reported in the literature for the systems considered in this study. We note that the phase segregation changes indicated in this Figure are similar to the phase segregation changes that we have observed in this work, namely: coarsening of phase domains in P3HT:fullerene system and decrease in the size of domains in PTB7:fullerene and PTB7-Th:fullerene systems. Additionally, we note as highlighted in Figure 6, that the length scales of the BHJ network and changes using DIO/thermal annealing produce stark changes in the PCE of the corresponding devices. Therefore, our results clearly show that SANS data can be used to choose the most promising morphologies for highly efficient OPV devices.

4. Conclusions

In this work, we have used a combination of SANS and AFM to study the morphological impact of the additive DIO on the following bulk-heterojunctions: P3HT:PC₇₁BM; PTB7:PC₇₁BM and PTB7-Th:PC₇₁BM. Our results help clarify some contradictory results found in the literature, by demonstrating that DIO acts as a type I additive (increases phase separation) in the P3HT:PC₇₁BM system, and as a type II additive (decreases oversized phase separation) in the PTB7:PC₇₁BM and PTB7-Th:PC₇₁BM systems. More importantly, this work highlights the potential of SANS as a powerful technique to probe the bulk morphology of BHJs, especially for detecting minor differences in morphology, such as the few nanometres change in the size of the phase domains in the P3HT:PC₇₁BM system, which are hardly detectable using AFM but which have a significant impact on device efficiency. Additionally, this work shows that the morphological information obtained with SANS can be used to select the BHJs with the highest potential for high performance OPVs. Finally, it is our expectation that this work can contribute to a more frequent and generalized use of SANS in the probing of the morphology of these systems.

Acknowledgments

This work was financially supported by project UID/EQU/00511/2019 - Laboratory for Process Engineering, Environment, Biotechnology and Energy – LEPABE funded by national funds through FCT/MCTES (PIDDAC). G.B. also thanks the European Commission for a Marie Skłodowska Curie Individual Fellowship (FP7/H2020 – Grant agreement number: 658391). G.P. thanks the National Council of Science and Technology (CONACyT) of Mexico and the Mexico Secretary of Energy (SENER) for the provision of a PhD scholarship. The authors thank Dr Sarah Rogers (ISIS Facility) for performing the SANS2D measurements. The STFC and the ISIS Pulsed Neutron Source are thanked for the provision of neutron beam time on LOQ (Experiments RB1620335 and RB1710364) and SANS2D (Xpress experiment XB1790087). This work benefited from the use of the SasView application, originally developed under NSF award DMR-0520547. SasView contains code developed with funding from the European Union's Horizon 2020 research and innovation programme under the SINE2020 project, grant agreement No 654000.

TABLES

Table 1. P3HT:PC71BM system: Scaling factors (C_{DAB}) and correlation lengths (L) obtained by fitting the experimental SANS data using the Debye-Anderson-Brumberger (DAB) model in the interval $q=0.008 - 0.1 \text{ \AA}^{-1}$.

P3HT:PC₇₁BM (DAB model)	C_{DAB}	L (\AA)	(χ^2/Npts)
No DIO, No TA	$7.29 \times 10^{-7} \pm$ 1.60×10^{-7}	40.9 ± 7.8	0.61
3% DIO, No TA	$22.2 \times 10^{-7} \pm$ 1.09×10^{-7}	57.4 ± 4.1	0.43
3% DIO, 5 min TA	$28.5 \times 10^{-7} \pm$ 1.04×10^{-7}	64.0 ± 3.7	1.05

Table 2. PTB7:PC₇₁BM system: **(Top)** Scaling factors (C_{DAB}) and correlation lengths (L) obtained by fitting the experimental SANS data from the samples processed with DIO with the Debye-Anderson-Brumberger (DAB) model in the interval $q=0.008 - 0.1 \text{ \AA}^{-1}$; **(Middle)** Effective volume fraction (ϕ_s), sphere diameter ($2R$) and polydispersity ratio obtained by fitting the experimental SANS data from the sample processed without DIO with the sphere model; **(Bottom)** scale factor (C_{SD}), dimensionality parameter (γ) and peak position (q_0) obtained by fitting the experimental SANS data from the sample processed without DIO with the spinodal model.

PTB7:PC₇₁BM (DAB model)	C_{DAB}	L (\AA)	(χ^2/Npts)
No DIO, No TA	-----	-----	-----
3% DIO, No TA	$72.6 \times 10^{-7} \pm$ 1.50×10^{-7}	37.9 ± 0.5	0.76
3% DIO, 5 min TA	$78.0 \times 10^{-7} \pm$ 0.79×10^{-7}	56.0 ± 0.5	4.03

PTB7:PC₇₁BM (Sphere model)	ϕ_s	$2R$ (\AA)	PD (ratio)	(χ^2/Npts)
No DIO, No TA Q = 0.008 – 0.254	$2.506 \times 10^{-5} \pm$ 3.652×10^{-6}	1822 ± 138	-----	0.84
No DIO, No TA Q = 0.0016 – 0.49	3.684×10^{-4}	1826 ± 26	0.33	4.67

PTB7:PC₇₁BM (Spinodal model)	C_{SD}	γ	q_0	(χ^2/Npts)
No DIO, No TA Q = 0.0016 – 0.49	14.97	4.46	0.0012	3.01

Table 3. PTB7-Th:PC₇₁BM system: **(Top)** Scaling factors (C_{DAB}) and correlation lengths (L) obtained by fitting the experimental data using the Debye-Anderson-Brumberger (DAB) model in the q intervals indicated; **(Bottom)** Scaling factor, gamma and q_0 obtained by fitting the experimental data using the spinodal model.

PTB7-Th:PC₇₁BM (DAB model)	q range (\AA^{-1})	C_{DAB}	L (\AA)	($\chi^2/$ Npts)
No DIO, No TA	0.008 – 0.254	$4.36 \times 10^{-7} \pm$ 1.07×10^{-8}	176.3 ± 9.4	1.07
	0.0016 – 0.49	$4.72 \times 10^{-7} \pm$ 4.77×10^{-9}	235.3 ± 3.1	4.37
3% DIO, No TA	0.008 – 0.1	$27.0 \times 10^{-7} \pm$ 1.26×10^{-7}	37.2 ± 1.1	0.50
3% DIO, 5 min TA	0.008 – 0.1	$35.4 \times 10^{-7} \pm$ 6.93×10^{-8}	52.0 ± 0.9	2.22

PTB7-Th:PC₇₁BM (Spinodal model)	C_{SD}	γ	q_0	($\chi^2/$ Npts)
No DIO, No TA 0.0016 – 0.49	1.51	3.44	0.0033	1.39

FIGURES

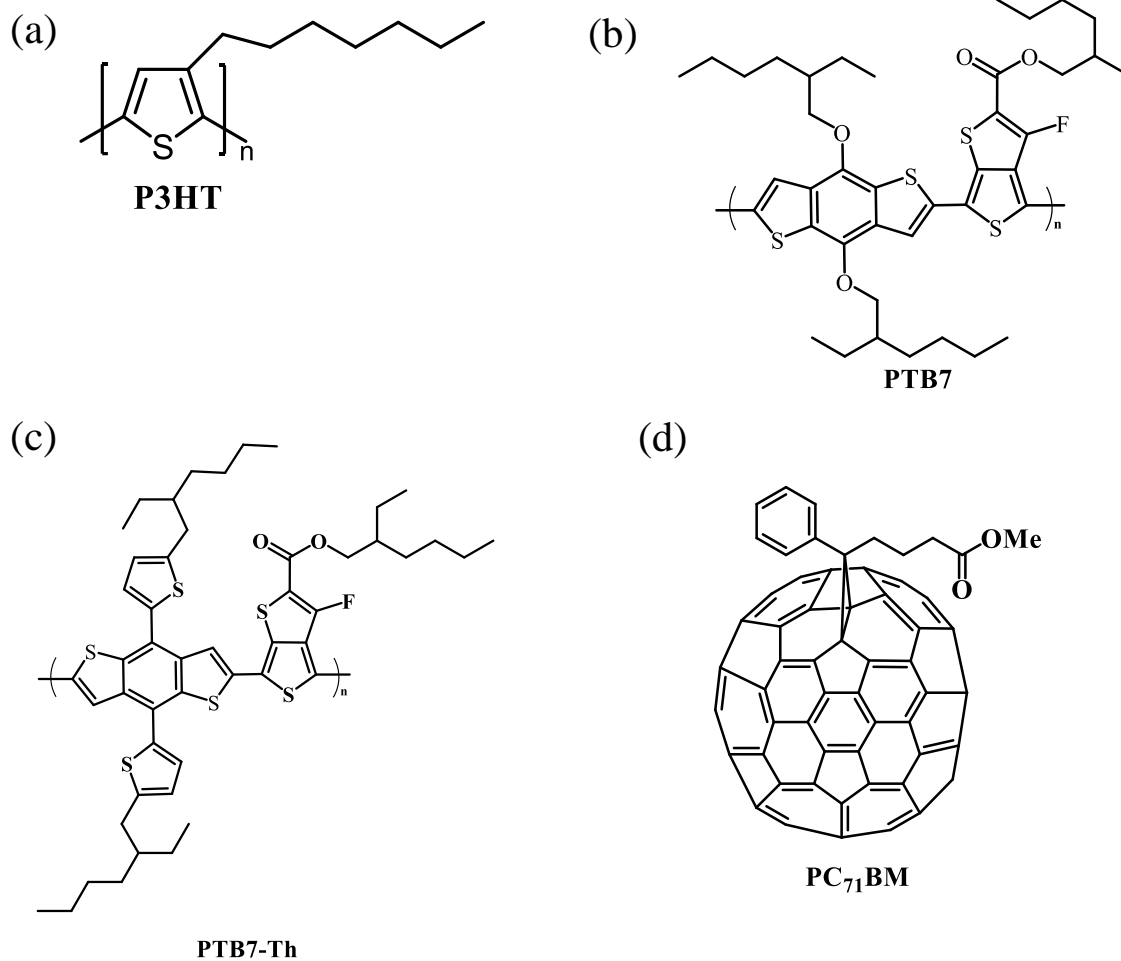
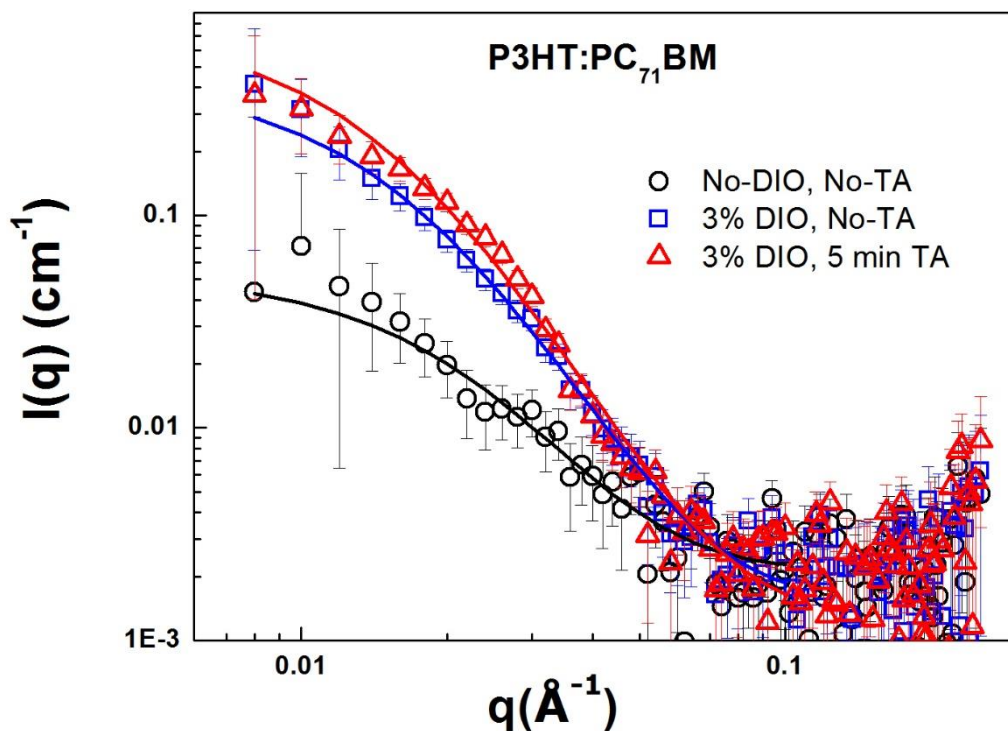


Figure 1. Chemical structures of: (a) P3HT; (b) PTB7; (c) PTB7-Th; (d) PC₇₁BM

(a)



(b)

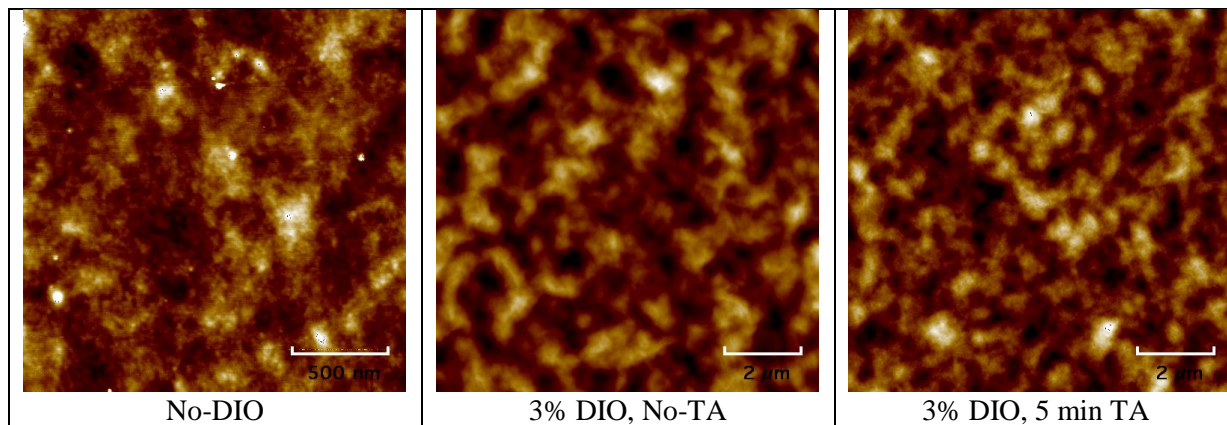
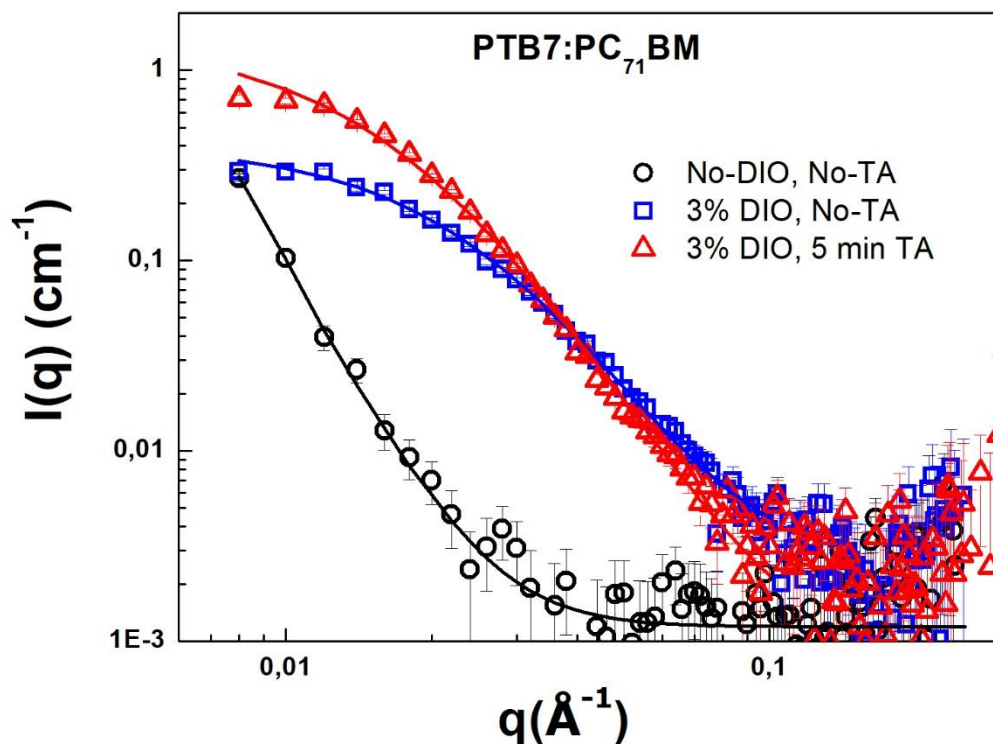


Figure 2. SANS data from P3HT:PC₇₁BM (3:2) blend films as measured on LOQ. As spun from chlorobenzene without DIO (black circles); as spun from chlorobenzene with 3% DIO (blue squares); spun from chlorobenzene with 3% DIO and post-annealed 5 minutes at 100 °C (red triangles). Model fits to the data using the DAB model are shown as solid lines. All the samples were completely dried under UHV ($\sim 5 \times 10^{-6}$ mbar) before the SANS measurements. (b) AFM images of the same P3HT:PC₇₁BM bulk heterojunction films.

(a)



(b)

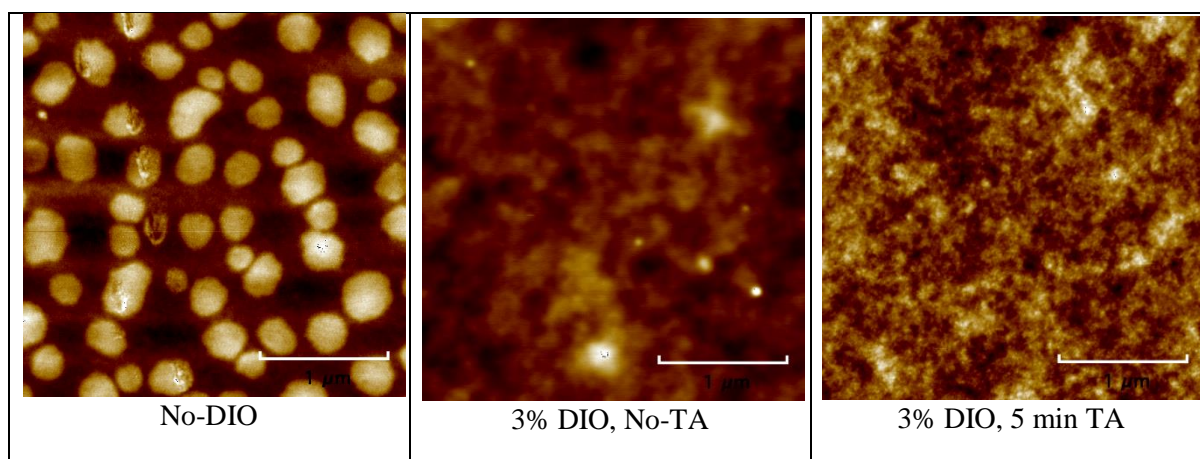


Figure 3. (a) SANS data from PTB7:PC₇₁BM (1:1.5) blend films as measured on LOQ. Processed from chlorobenzene: without DIO (black circles); with 3% DIO (blue squares); with 3% DIO and post-annealed 5 minutes at 100 °C (red triangles). All the samples were completely dried under UHV ($\sim 5 \times 10^{-6}$ mbar) before SANS measurements. Data without DIO (black line) was fitted with a sphere model; data with DIO (blue and red lines) were fitted with the DAB model (b) AFM images of the same PTB7:PC₇₁BM bulk heterojunction films.

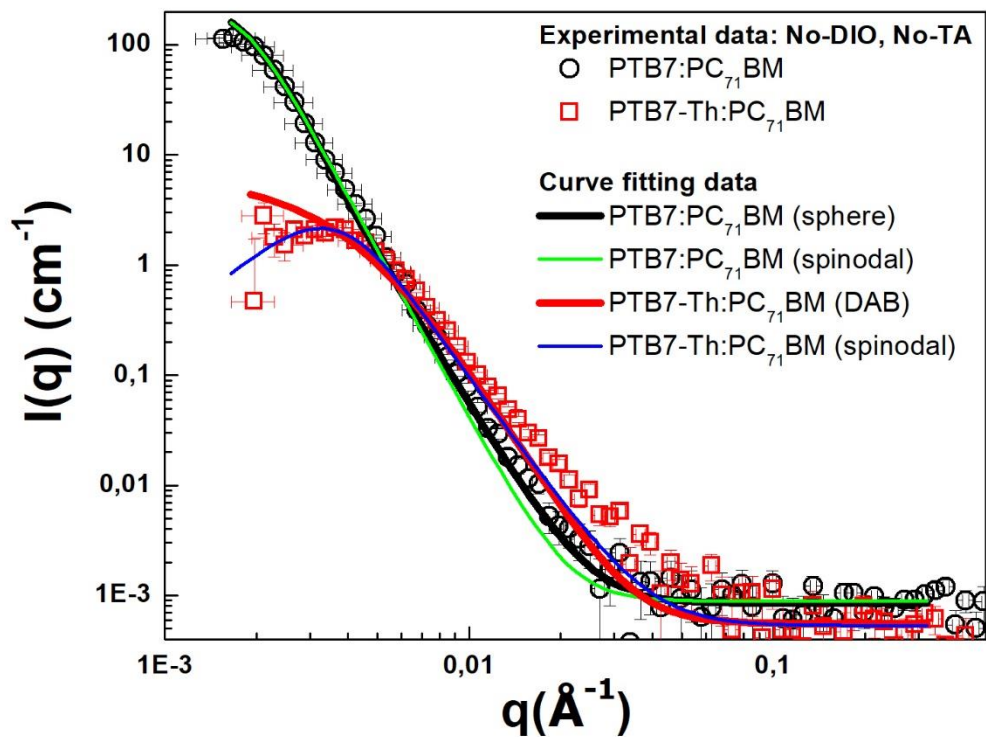
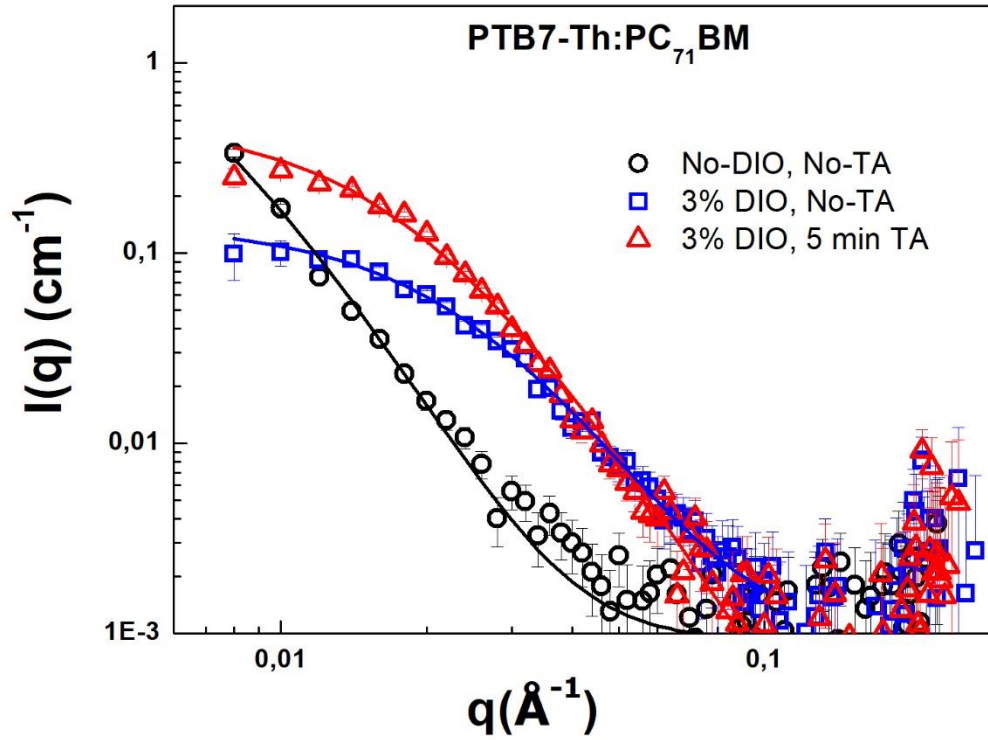


Figure 4. SANS data, measured on SANS2D, from PTB7:PC₇₁BM (black open circles) and PTB7-Th:PC₇₁BM (red open squares) blend films as spun cast from chlorobenzene without DIO and without annealing. The solid lines are fits to the models shown in the legend.

(a)



(b)

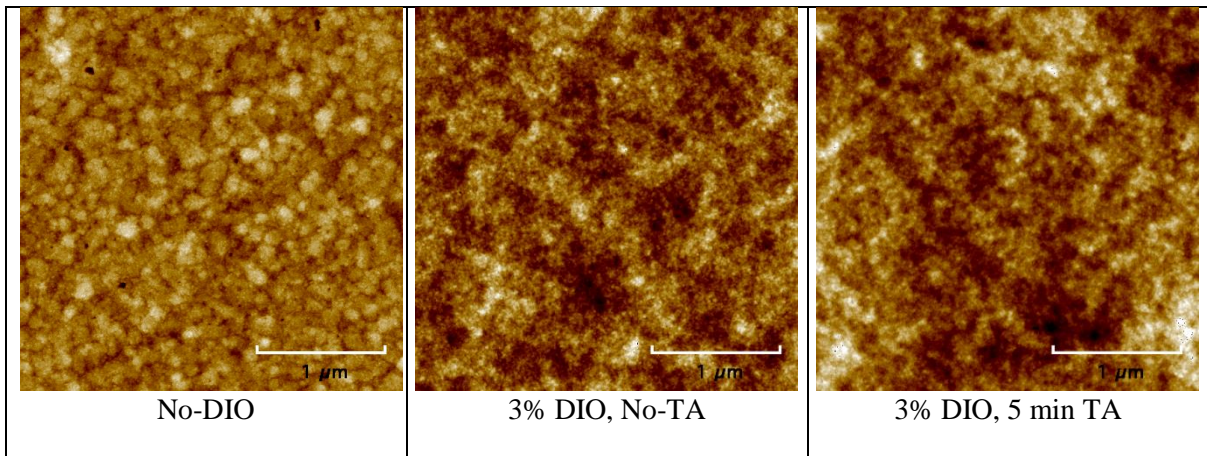


Figure 5. SANS data from PTB7-Th:PC₇₁BM (1:1.5) blend films as measured on LOQ. Processed from chlorobenzene: without DIO (black circles); with 3% DIO (blue squares); with 3% DIO and post-annealed 5 minutes at 100 °C (red triangles). All the samples were completely dried under UHV (~5x10⁻⁶ mbar) before SANS measurement. The solid lines are DAB model fits to the data. (b) AFM images of the same PTB7-Th:PC₇₁BM bulk heterojunction films.

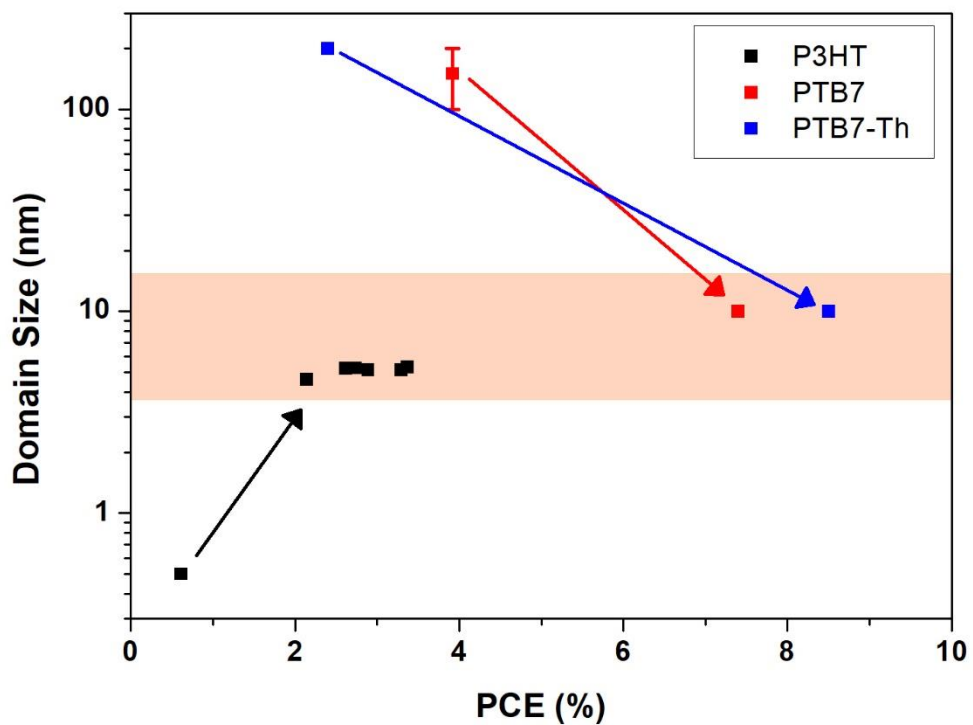


Figure 6. Correlation between the size of polymer:fullerene phase domains and the efficiency of the corresponding devices as reported in the literature for BHJs with the polymers P3HT [35], PTB7 [21] and PTB7-Th [24]. The orange band indicates the typical domain size range required for highly efficient OPV devices and is dictated by the exciton diffusion length in OPVs which is ~ 10 nm [40, 41].

References

1. Cheng, P., et al., *Next-generation organic photovoltaics based on non-fullerene acceptors*. Nature Photonics, 2018. **12**(3): p. 131-142.
2. Zhang, J., et al., *Material insights and challenges for non-fullerene organic solar cells based on small molecular acceptors*. Nature Energy, 2018. **3**(9): p. 720-731.
3. Hou, J., et al., *Organic solar cells based on non-fullerene acceptors*. Nature Materials, 2018. **17**: p. 119.
4. Gaspar, H., et al., *Recent Developments in the Optimization of the Bulk Heterojunction Morphology of Polymer: Fullerene Solar Cells*. Materials, 2018. **11**(12).
5. Sondergaard, R., et al., *Roll-to-roll fabrication of polymer solar cells*. Materials Today, 2012. **15**(1-2): p. 36-49.
6. Xiao, Z., X. Jia, and L.M. Ding, *Ternary organic solar cells offer 14% power conversion efficiency*. Science Bulletin, 2017. **62**(23): p. 1562-1564.
7. Li, S.S., et al., *A Wide Band Gap Polymer with a Deep Highest Occupied Molecular Orbital Level Enables 14.2% Efficiency in Polymer Solar Cells*. Journal of the American Chemical Society, 2018. **140**(23): p. 7159-7167.
8. Cui, Y., et al., *Over 16% efficiency organic photovoltaic cells enabled by a chlorinated acceptor with increased open-circuit voltages*. Nature Communications, 2019. **10**(1): p. 2515.
9. Meng, L.X., et al., *Organic and solution-processed tandem solar cells with 17.3% efficiency*. Science, 2018. **361**(6407): p. 1094-+.
10. Zhang, Y.W., et al., *Comparative indoor and outdoor stability measurements of polymer based solar cells*. Scientific Reports, 2017. **7**.
11. Zhan, X.W. and D.B. Zhu, *Conjugated polymers for high-efficiency organic photovoltaics*. Polymer Chemistry, 2010. **1**(4): p. 409-419.
12. Sun, H., F. Chen, and Z.K. Chen, *Recent progress on non-fullerene acceptors for organic photovoltaics*. Materials Today, 2019. **24**: p. 94-118.
13. Liao, H.-C., et al., *Additives for morphology control in high-efficiency organic solar cells*. Materials Today, 2013. **16**(9): p. 326-336.
14. McDowell, C., et al., *Solvent Additives: Key Morphology-Directing Agents for Solution-Processed Organic Solar Cells*. Advanced Materials, 2018. **30**(33): p. 1707114.
15. Bernardo, G., et al., *Does 1,8-diiodooctane affect the aggregation state of PC71BM in solution?* Royal Society Open Science, 2018. **5**(9): p. 180937.
16. Bernardo, G., et al., *Data from: Does 1,8-Diiodooctane affect the aggregation state of PC71BM in solution?*, in *Dryad Digital Repository*. 2018.
17. Zhang, Y., et al., *Understanding and controlling morphology evolution via DIO plasticization in PffBT4T-2OD/PC71BM devices*. Scientific Reports, 2017. **7**: p. 44269.
18. Arca, F., M. Loch, and P. Lugli, *Enhancing Efficiency of Organic Bulkheterojunction Solar Cells by Using 1,8-Diiodooctane as Processing Additive*. Ieee Journal of Photovoltaics, 2014. **4**(6): p. 1560-1565.
19. Jang, W., et al., *Morphological engineering via processing additive in thin film bulk-heterojunction photovoltaic cells: A systematic understanding of crystal size and charge transport*. Current Applied Physics, 2016. **16**(10): p. 1424-1430.
20. Long, Y., et al., *Effect of a high boiling point additive on the morphology of solution-processed P3HT-fullerene blends*. Synthetic Metals, 2016. **216**: p. 23-30.
21. Liang, Y., et al., *For the Bright Future—Bulk Heterojunction Polymer Solar Cells with Power Conversion Efficiency of 7.4%*. Advanced Materials, 2010. **22**(20): p. E135-E138.
22. Huang, D., et al., *Enhanced performance and morphological evolution of PTB7:PC71BM polymer solar cells by using solvent mixtures with different additives*. Physical Chemistry Chemical Physics, 2015. **17**(12): p. 8053-8060.

23. Wan, Q., et al., *10.8% Efficiency Polymer Solar Cells Based on PTB7-Th and PC71BM via Binary Solvent Additives Treatment*. *Advanced Functional Materials*, 2016. **26**(36): p. 6635-6640.
24. Xie, Y., et al., *Butanedithiol Solvent Additive Extracting Fullerenes from Donor Phase To Improve Performance and Photostability in Polymer Solar Cells*. *ACS Applied Materials & Interfaces*, 2017. **9**(11): p. 9918-9925.
25. Huang, W., et al., *Influence of Fullerene Acceptor on the Performance, Microstructure, and Photophysics of Low Bandgap Polymer Solar Cells*. *Advanced Energy Materials*, 2017: p. 1602197-n/a.
26. Yin, W. and M. Dadmun, *A New Model for the Morphology of P3HT/PCBM Organic Photovoltaics from Small-Angle Neutron Scattering: Rivers and Streams*. *ACS Nano*, 2011. **5**(6): p. 4756-4768.
27. Chen, H., et al., *Correlation of polymeric compatibilizer structure to its impact on the morphology and function of P3HT:PCBM bulk heterojunctions*. *Journal of Materials Chemistry A*, 2013. **1**(17): p. 5309-5319.
28. Zhang, Y., et al., *Effect of fullerene acceptor on the performance of solar cells based on PffBT4T-2OD*. *Physical Chemistry Chemical Physics*, 2018. **20**(28): p. 19023-19029.
29. Fernandes, L., et al., *Thermal stability of low-bandgap copolymers PTB7 and PTB7-Th and their bulk heterojunction composites*. *Polymer Bulletin*, 2018. **75**(2): p. 515-532.
30. Heenan, R.K., J. Penfold, and S.M. King, *SANS at pulsed neutron sources: Present and future prospects*. *Journal of Applied Crystallography*, 1997. **30**: p. 1140-1147.
31. Heenan, R., et al., *SANS2D at the ISIS Second Target Station*. 2006.
32. Akeroyd, F., et al. *Mantid: Manipulation and Analysis Toolkit for Instrument Data*. 2013 [cited 2016 20/07]; Available from: <http://dx.doi.org/10.5286/SOFTWARE/MANTID>.
33. Wignall, G.D. and F.S. Bates, *Absolute Calibration of Small-Angle Neutron-Scattering Data*. *Journal of Applied Crystallography*, 1987. **20**: p. 28-40.
34. Alina, G., et al. *SasView for Small Angle Scattering Analysis*. Date of access: 20/07/2016]; Available from: <http://www.sasview.org/>.
35. Chen, D., et al., *P3HT/PCBM Bulk Heterojunction Organic Photovoltaics: Correlating Efficiency and Morphology*. *Nano Letters*, 2011. **11**(2): p. 561-567.
36. Li, N., et al., *Abnormal strong burn-in degradation of highly efficient polymer solar cells caused by spinodal donor-acceptor demixing*. *Nature Communications*, 2017. **8**(1): p. 14541.
37. Hynes, E.L., et al., *Interfacial width and phase equilibrium in polymer-fullerene thin-films*. *Communications Physics*, 2019. **2**(1): p. 112.
38. Furukawa, H., *Dynamics-scaling theory for phase-separating unmixing mixtures: Growth rates of droplets and scaling properties of autocorrelation functions*. *Physica A: Statistical Mechanics and its Applications*, 1984. **123**(2): p. 497-515.
39. Parnell, A.J., et al., *Depletion of PCBM at the Cathode Interface in P3HT/PCBM Thin Films as Quantified via Neutron Reflectivity Measurements*. *Advanced Materials*, 2010. **22**(22): p. 2444-+.
40. Menke, S.M. and R.J. Holmes, *Exciton diffusion in organic photovoltaic cells*. *Energy & Environmental Science*, 2014. **7**(2): p. 499-512.
41. Luhman, W.A. and R.J. Holmes, *Investigation of Energy Transfer in Organic Photovoltaic Cells and Impact on Exciton Diffusion Length Measurements*. *Advanced Functional Materials*, 2011. **21**(4): p. 764-771.